This is a preprint, the final version is subject to change, of the American Mineralogist (MSA)
Cite as Authors (Year) Title. American Mineralogist, in press.
DOI: https://doi.org/10.2138/am-2019-6996

[*Revision 1*]The role of mineral nanoparticles at a fluid-magnetite interface: Implications for trace-element uptake in hydrothermal systems

Shuo Yin[1, 2]*, Richard Wirth[2], Changqian Ma[1]*, Jiannan Xu[1]

1 State Key Laboratory of Geological Process and Mineral Resources, School of Earth Sciences, China University of Geosciences, Wuhan, Hubei, 430074, P.R. China

2 GFZ German Research Centre for Geosciences, Section 3.5: Interface Geochemistry, Telegrafenberg, 14473 Potsdam, Germany

Shuo Yin: yinshuo1128@126.com

Richard Wirth: wirth@gfz-potsdam.de

Changqian Ma: cqma@cug.edu.cn

Jiannan Xu: jnxu@gmail.com

Abstract

The migrating fluid-mineral interface provides an opportunity for the uptake of trace elements as solid solutions in the newly formed crystal lattice during the non-equilibrium growth of the crystal. However, mineral nanoparticles could precipitate directly from the interfacial fluid when it evolves to a supersaturated situation. To better understand the role of mineral nanoparticles in this scenario, this study focuses on a well-documented magnetite with oscillatory zoning from a skarn deposit by using high-resolution transmission electron microscopy (TEM). Our results show that the Al concentration in

magnetite measured on a micron-scale is caused by three different effects: Al solid solution, Al-rich nanometer-sized lamellae and zinc spinel nanoparticles in the host magnetite. Here, we propose a genetic relationship among the three different phases mentioned above. At first, a continuous increase of the Al concentration in the interfacial fluid can be incorporated into the crystal lattice of magnetite forming a solid solution. During cooling in a later stage, aluminum in magnetite is oversaturated and exsolution of hercynite (Al-rich lamellae) occurs from the host magnetite. If the Al concentration at the fluid-magnetite interface still increases during further growth of magnetite, the substitution of Fe by Al has gradually reached saturation so that aluminum cannot be incorporated in the magnetite crystal structure any longer. Using the magnetite lattice as a template, nucleation of abundant zinc spinel nanoparticles occurs. This will in turn lead to a gradual depletion of Al concentration in the interfacial fluid until the available ions for zinc spinel nucleation and growth have been used up. As a result, the migrating fluid-magnetite interface will enrich the Al concentration in the interfacial fluid until the available ion concentration is sufficient for nucleation of zinc spinel phase again. The fluid-mineral interface in this mechanism has been repeatedly utilized during crystal growth, providing an efficient way for the uptake of trace element from a related undersaturated bulk fluid.

Keywords: fluid-mineral interface, mineral nanoparticle, hydrothermal magnetite, uptake of trace element

Introduction

The partition coefficient of a certain trace element between the bulk fluid and the bulk crystal can be determined in controlled experiments under a steady-state condition. The incompatibility or compatibility of such a trace element in a mineral can thus be used to determine its geochemical behavior in natural systems. However, the fluid-mineral interfaces generally have a composition that differs from that of the bulk fluid or the bulk crystal (Brown, 2001; Fenter and Sturchio, 2004; Stipp, 1999). The interfacial fluid composition could be recorded by the newly formed crystal lattice when the crystal growth rate is fast enough, leading to deviations from thermodynamic partitioning equilibrium (Watson, 1996; Watson, 2004). This kinetic control on the uptake of trace elements induced by the crystal growth rate is so called the growth entrapment model (Lanzillo et al., 2014).

The formation of a sharp compositional boundary between a trace element-poor domain and a trace element-rich domain is suggested to form in this model when the crystal growth rate is fast enough. This signature will be further preserved when it is not eliminated by the intracrystalline diffusion, which is a function of the temperature. Specifically, a trace element-rich domain in a host mineral can contain some mineral nanoparticles when the local fluid is supersaturated with respect to a new phase (Deditius et al., 2018).

To better understand the role of mineral nanoparticles at a fluid-mineral interface,

this study focuses on a well-documented magnetite grain with oscillatory zoning from the Baishiya skarn iron deposit, East Kunlun orogenic belt, northern Qinghai-Tibet Plateau. Using high-resolution transmission electronic microscopy (TEM), we have observed Al-rich nanometer scale lamellae, Ti-rich magnetite nanoparticles and zinc spinel nanoparticles in the host magnetite. An integrated study from a micron scale to a nanometer scale is focused on: 1) genesis of mineral nanoparticles in hydrothermal magnetite; 2) explanation why zinc prefers to form zinc spinel nanoparticles rather than be incorporated into the magnetite structure thus forming a solid solution; 3) a potential mechanism for the uptake of trace elements at a fluid-mineral interface in hydrothermal deposits.

Geological setting and sample description

The East Kunlun orogenic belt in the northern Qinghai-Tibet Plateau consists of multistage granitoid batholiths (Fig. 1a), and is dominated by Late Paleozoic to early Mesozoic granitoids (Fig. 1b). The magmatic-hydrothermal deposits are mainly associated with the Triassic magmatism induced by the northward subduction of the Songpan-Ganzi-Bayan Har block. The Baishiya skarn iron deposit, located in the uplift edge of the Dulan-Elashan belt, is hosted by the Triassic granodiorite and the limestone in the Dagangou Formation (Fig. 1c). There is a discontinuous mineralized contact zone approximately 2000 m long and 50-300 m wide, with a proven reserve of 8 Mt Fe at an average grade of 35–51 % Fe.

The magnetite sample was collected from the Baishiya skarn iron deposit, providing a unique opportunity to investigate trace element behavior in hydrothermal magnetite at a nanometer scale. The magnetite ores in the Baishiya skarn deposit have previously been identified with four generations based on in-situ textures and trace elements analyses, as well as gangue mineral assemblage (Yin et al., 2017). In particular, the studied magnetite crystal coexisting with phlogopite and minor hedenbergite is characterized by a homogeneous core and an oscillatory rim in the backscattered electron image (Fig. 2). This special texture is a perfect record of the migrating fluid-mineral interface during non-equilibrium crystal growth.

Trace element concentrations have been determined in this magnetite crystal by electron microprobe and laser ablation inductively coupled plasma mass spectrometry (LA-ICP-MS) (Yin et al., 2017). They are plotted in the order of increasing compatibility in the magnetite structure (Fig. 3; Dare et al., 2014). In comparison with the homogeneous core, the oscillatory rim has significantly higher concentrations of Si, Al, Mg, Zn and lower concentrations of Ti, V, and Ni.

Analytical methods

Electron-transparent foils for TEM were prepared by focused ion beam technique (FIB), utilizing a single-beam device (FEI FIB200 TEM) and a state-of-the-art DualBeam™ system (FEI Helios) operated at German Research Center for Geosciences, Potsdam. The foils have been cut by FIB along the growth direction of magnetite to

investigate the phase variation on a nanometer scale (Fig. 2d). The foil thickness is approximately less than ~100-150 nm. Details about the FIB sample preparation from magnetite can be found elsewhere (Wirth, 2009). The TEM was performed employing a TECNAI F20 X-Twin transmission electron microscope operated at 200 keV with a Schottky emitter as electron source. Using scanning transmission mode, annular-dark field (STEM-ADF) images and some EDS maps were acquired with a JEOL JEM-Arm300F at 300 keV acceleration voltage and a cold field emission gun (FEG) emitter as an electron source (JEOL Application laboratory, Tokyo, Japan). The TECNAI was equipped with a Gatan imaging filter, a Fishione high-angle annular dark-field detector (HAADF) and an energy dispersive X-ray (EDX) analyzer with ultrathin detector window. The HAADF detector can be operated as a Z-contrast detector using a short camera length (75mm) or as a combined Z-contrast plus diffraction contrast sensitive detector (camera length 330 mm). TEM bright-field and dark-field images, as well as high-resolution lattice fringe images, were routinely acquired as energy-filtered images applying a 20 eV window to the zero-loss peak. High-resolution images were used to calculate diffraction patterns by Fast Fourier Transform (FFT). EDX analyses usually have been carried out in the STEM thus avoiding mass loss during data acquisition. Lines scans and elemental mapping have been acquired using the corresponding X-Ray intensities.

Results

4.1 Nanometer-sized Al-Mg-rich lamellae in magnetite

The Al-Mg-rich lamellae (approximately 100 nm × 3 nm) are documented in STEM-ADF image (Fig. 4). Element mapping and line scans across the lamellae show that the thin lamellae are enriched in Al, Mg, Ti, and depleted in Fe compared with the host magnetite (Fig. 4). Calculated diffraction patterns from the HAADF images show a split of the second order reflection of the (111) reflections, suggesting the presence of two different spinel crystals with slightly different unit cell parameters ($a_{0\ hercynite}$ = 0.8119 nm; $a_{0\ magnetite}$ = 0.8387 nm (MinDat.org)). This scenario is in accordance with the separation of the (222) reflections of the reciprocal lattice in Fig. 7a, in which the inner spot is 0.24211 nm for $(222)_{magnetite}$ and the outer spot is 0.23438 nm for $(222)_{hercynite}$. Consequently, the Al-Mg-rich lamellae are a hercynite phase that has exsolved from the host magnetite, in which iron and aluminum have been partly substituted by Mg and Ti, respectively.

4.2 Zinc spinel nanoparticles in magnetite

High-resolution TEM study revealed several crystalline inclusions up to 100 nm in size, and most of which have an irregular cross-section (Fig. 9). X-ray maps of these inclusions show a pronounced enrichment of Zn and Al and concomitant depletion of Fe compared with the host magnetite (Fig. 5). A slight enrichment of Mg content has also been observed in some cases (Fig. 6). In a few cases, a decrease of oxygen (Kα) X-ray intensity together with a decrease of intensities from other elements suggests the

existence of pores once filled with a fluid (Fig. 6). The fluid phase was trapped in the pores and then released during FIB milling. The pore (~5 nm) seems to be inside the zinc spinel phase. It is much smaller than the thickness of the TEM foil (~100 nm). Again, there is a splitting in the third order reflections of the (111) diffraction spots in the diffraction pattern (FFT) between the Zn-Al-rich nanoparticle and the host magnetite (Fig. 7b), indicating the same crystal structure with only slightly deviating lattice parameters of the zinc spinel phase from that of the host magnetite.

4.3 Titanium-rich magnetite nanocrystals in magnetite

Occasionally, we have also observed some individual Ti-rich nanoparticles with 5-30 nm in cross section (Fig. 4, 6). They are either Ti-rich magnetite or ulvöspinel due to undistinguishable lattice parameters (Fig. 7b). Host magnetite and ulvöspinel have the same cubic crystal structure and similar unit cell parameters ($a_{0\ \text{ulvöspinel}} = 0.845$ nm; $a_{0\ \text{magnetite}} = 0.8387$ nm (MinDat.org)). The Ti concentration in the dark zone of magnetite approximately ranges from 10 ppm to 100 ppm on a micron scale by LA-ICP-MS (Fig. 2). Even in the trace element-rich domain on a nanometer scale, it is below the detection limit by EDX analysis in the magnetite matrix. Thus, the Ti-rich nanoparticles are unlikely to be exsolution of ulvöspinel from the host magnetite (Lilova et al., 2012). On the contrary, previous study suggested that Ti is an incompatible element in magnetite structure at middle to lower temperature (e.g., 390 °C; Nadoll et al., 2017). It will be enriched in the interfacial fluid due to migrating magnetite/fluid interface of the growing

magnetite. Once the Ti concentration reaches to a supersaturated situation, nucleation of Ti-rich magnetite nanoparticles occurs.

Discussion

The exsolution of a hercynite phase

At a temperature below 600 °C, such as a skarn environment, the threshold value ($Magentite_{90}Hercynite_{10}$) for hercynite exsolution in magnetite structure is that the Al content reaches approximately 1.2 wt.% (Fig. 8) (Turnock and Eugster, 1962). This critical value could be comparable to our "mixed" result in the magnetite matrix (Fig. 3). In fact, an exsolution of nanoscale hercynite from magnetite had long been observed in geological samples. For example, Al-Mn-Fe-bearing spinel nanoplates have been found in metamorphic magnetite crystals with the Al concentration up to 1.04 wt.% (Sitzman et al., 2000). Hydrothermal magnetite crystal with 2-3 wt.% of Al from the Los Colorados iron oxide-apatite deposit also contains nanoscale hercynite-rich domains (Deditius et al., 2018). Most of these hercynite lamellae have a thickness of a few nanometers and parallel to a certain orientation, which is consistent with our observation of the Al-Mg-rich lamellae in this study. Consequently, it is reasonable to conclude that the Al-Mg-rich lamellae are hercynite phases exsolved from the host magnetite.

Nucleation of aluminous spinel nanoparticles at the fluid-magnetite interface

Oscillatory zoning is a common feature of natural crystal growth. It can form by a

rapid depletion and subsequent increase of some chemical components at a fluid-mineral interface (Putnis et al., 1992). For magnetite precipitated from a hydrothermal fluid, it also requires that the magnetite growth rate is high enough relative to the intracrystalline diffusion rate (temperature-dependent) so that the sharp boundaries of the original zoning will be preserved (Deditius et al., 2018; Watson, 2004). Regardless of the magnetite growth rate, the Al concentration in the newly formed magnetite lattice are controlled by two effects. The first one is the intracrystalline diffusion rate of Al between the newly formed magnetite lattice and bulk magnetite crystal (Watson, 2004). Because the newly formed magnetite lattice precipitated directly from the interfacial fluid, the diffusion rate of Al between the interfacial fluid layer and the bulk fluid is also a crucial factor (Watson and Müller, 2009).

As an incompatible element in magnetite structure, aluminum prefers to remain in the fluid phase, leading to a continuous enrichment of the Al concentration at the moving fluid-magnetite interface. This will in turn result in an increased adsorption of Al^{3+} at the mobile magnetite surface, which will be incorporated into the newly formed magnetite lattice by rapid magnetite growth (Watson, 2004). If the Al concentration in the magnetite surface structure continues to increase, hercynite exsolution occurs during the late stage of cooling due to a limited solid solution for Al substitution in the magnetite structure (Phase 1; Fig. 9).

The radius of Al^{3+} ion (0.54 Å) is smaller than that of Fe^{3+} ion (0.65 Å) (Dare et al., 2012). An increase of this substitution by Al will lead to a corresponding increase of the

free energy of the magnetite structure due to this mismatch in crystal lattice. Once the replacement of Fe by Al in the magnetite surface structure has reached a maximum value (Fig. 8), additional Al^{3+} will not be incorporated into the newly formed magnetite lattice any longer, but enriched in the interfacial fluid. An aluminous spinel nucleus with a few nanometers in size will directly form at the magnetite surface using the magnetite crystal lattice as a template for nucleation. The reason is that the nucleating aluminous spinel phase closely matches with the atomic structure of the magnetite lattice so that the lattice strain energy is minimized by this way. In other words, in comparison with Al-spinel precipitated from a fluid phase (Fig. 10), the "critical size" for a stable nucleus that has used magnetite as a template for nucleation should be reduced to some extent. In fact, this chemically tailored substrate has been routinely used to modify energy landscape at the substrate/nucleus interface and thereby steer heterogeneous nucleation in the biological and artificial mineralization experiments (De Yoreo and Vekilov, 2003; Li et al., 2018).

The nucleation and growth of abundant Al-rich nanoparticles at the magnetite surface will not end until the available ions (e.g., Zn, Mg, Al) in the interfacial fluid have been used up. The concentration of the residual ions is not sufficient for a nucleus to exceed the "critical size" (Phase 2; Fig. 9). In other words, the nucleation process will gradually reduce the concentration of Al^{3+} in the interfacial fluid and finally lead to the absence of aluminous spinel at the moving fluid-magnetite interface, so as to a crystallization of relatively pure magnetite without aluminous spinel (Phase 3; Fig. 9).

Nucleation of aluminous spinel directly from a local fluid

In the model above, one may doubt that abundant aluminous nanoparticles are a direct result of the supersaturation of a local fluid, and then they have been enclosed by the growing magnetite. If this assumption is reasonable, they should have a random distribution of crystallographic orientation because they are isolated with each other, which is obviously contrary with our observation. Individual aluminous nanoparticles have been measured randomly in their electronic diffraction patterns. It turns out that they share a same crystallographic orientation with the host magnetite due to an extremely narrow d-spacings. For example, additional spots in the diffraction pattern of magnetite have never been observed using the TEM in GFZ, Potsdam. Even with a more advanced TEM (JEOL Application laboratory, Tokyo, Japan), a split can only be observed in the second order reflection (Fig. 7). This suggests that the atomic structure of aluminous spinel phase is closely matched with the host magnetite substrate.

Trace element behavior at a fluid-magnetite interface

Previous research generally considered that zinc is a compatible element in magnetite structure (Nadoll et al., 2014; Nadoll et al., 2017). However, the contrast of zinc concentration between the host magnetite and the aluminous spinel phase suggests a strongly preferential uptake of zinc by the aluminous spinel phase at a fluid-magnetite interface (Fig. 5-6). At a lower concentration of zinc in the host magnetite (Fig. 3), an intriguing question is why zinc prefers to form aluminous spinel nanoparticles rather than

being incorporated in magnetite structure as a solid solution.

The relationships among endmembers in the spinel group could account for this heterogeneous distribution of zinc at a fluid-magnetite interface. Specifically, franklinite ($ZnFe_2O_4$) can only form a partial solid solution with magnetite (Valentino et al., 1990). The intergrowth of franklinite-magnetite lamellae has been observed in natural samples (Valentino et al., 1990). However, there is a significant substitution among Zn, Mg and Fe in aluminous spinel (Heimann et al., 2005), presumably indicating complete solid solutions. As a result, it is reasonable to consider that the free energy of lattice strain induced by the Zn substitution for Fe should be lower in the $ZnAl_2O_4$–$FeAl_2O_4$ series than that of the $ZnFe_2O_4$–$FeFe_2O_4$ series. Thus, we consider that zinc should be more compatible with aluminous spinel than with magnetite in a hydrothermal fluid.

Once the nucleation and growth of zinc spinel phase occurs, it may also have an influence on other trace elements. For instance, there is also a slight enrichment of Mg in the zinc spinel nanoparticle, which is less pronounced than that of Zn and Al (Fig. 6). Previous research considered that magnesioferrite ($MgFe_2O_4$) phases can form a complete solid solution with magnetite (Dupuis and Beaudoin, 2011). If true, it means that the competition for Mg by aluminous spinel should be at the same level as that of magnetite. However, if the endmember of the aluminous spinel is zinc spinel, it turns out to be a competitive replacement by Mg^{2+} (0.72 Å) between Fe^{2+} (0.78 Å) and Zn^{2+} (0.74 Å) (Dare et al., 2012). The radius of Mg^{2+} is closer to Zn^{2+} rather than that of Fe^{2+}, which may be the reason for this slightly enrichment.

Implications

The zinc concentration in the bulk fluid should be lower than that in magnetite because Zn is a relatively compatible element in magnetite structure (Nadoll et al., 2014). It is consistent with the fact that zinc minerals are absent in the magnetite ores and the related thin sections, indicating a zinc-undersaturated bulk fluid phase. However, at a migrating fluid-magnetite interface, a continuous increase of the Al concentration allows the nucleation of a zinc spinel phase by utilizing magnetite as a template. This local kinetic effect has changed the reaction pathway of zinc, leading to the uptake of zinc from a zinc-undersaturated bulk fluid.

The uptake of trace elements at fluid-mineral interfaces by nanoparticles can be comparable to some mineral replacement experiments (Li et al., 2015; Tooth et al., 2011). However, there are some prominent characteristics in this study. First and foremost, the trigger of this local kinetic effect is the higher crystal growth rate relative to intracrystalline diffusion rate at a fluid-mineral interface, causing a gradual enrichment of trace elements in the interfacial fluid. Furthermore, once the available Zn^{2+} and Al^{3+} for the nucleation of a stable zinc spinel nanoparticle are exhausted in the interfacial fluid, a relatively pure magnetite crystallization will consume Fe and enrich available Zn^{2+} and Al^{3+} ions in the interfacial fluid again. The moving fluid-magnetite interface has been repeatedly utilized to nucleate zinc spinel during magnetite growth, which resembles a rhythmical distribution of pyrrhotite nanoparticles observed in a magmatic apatite

(Gottesmann and Wirth, 1997). Consequently, it is a potential mechanism for the uptake of trace element from an undersaturated bulk fluid. Finally, the host substrate could play a crucial role as a template in nucleating zinc spinel or mineral nanoparticles and thus have an influence on related trace element behavior, which might have been overlooked in hydrothermal systems. Such a new documentation of phenomena may be of broad relevance and importance for us to understand the growth of mineral nanoparticle (De Yoreo et al., 2015).

Acknowledgements

We thank Hang Zhang and Yuheng Guo for their assistance in the field and sample preparation, Anja Schreiber for FIB sample preparation, as well as a part of TEM result from JEOL Application Lab, Tokyo. We appreciate the associate editor Aaron Celestian for his handling of this manuscript, and feel grateful for constructive comments and editorial suggestions from E. Bruce Watson and an anonymous reviewer. This research was supported by the National Science Foundation of China (grant 41272079) and the National Basic Research Program of China (grant 2012CB416802).

References Cited

Brown, G.E. (2001) How minerals react with water. Science, 294, 67-69.

Dare, S.A.S., Barnes, S.-J., Beaudoin, G. (2012) Variation in trace element content of magnetite crystallized from a fractionating sulfide liquid, Sudbury, Canada:

Implications for provenance discrimination. Geochimica et Cosmochimica Acta, 88, 27-50.

Dare, S.A.S., Barnes, S.J., Beaudoin, G., Meric, J., Boutroy, E., and Potvin-Doucet, C. (2014) Trace elements in magnetite as petrogenetic indicators. Mineralium Deposita, 49, 785-796.

De Yoreo, J.J., and Vekilov, P.G. (2003) Principles of crystal nucleation and growth. Reviews in mineralogy and geochemistry, 54, 57-93.

De Yoreo, J.J., Gilbert, P.U., Sommerdijk, N.A., Penn, R.L., Whitelam, S., Joester, D., Zhang, H., Rimer, J.D., Navrotsky, A., Banfield, J.F., Wallace, A.F., Michel, F.M., Meldrum, F.C., Colfen, H., and Dove, P.M. (2015) Crystallization by particle attachment in synthetic, biogenic, and geologic environments. Science, 349, aaa6760.

Deditius, A.P., Reich, M., Simon, A.C., Suvorova, A., Knipping, J., Roberts, M.P., Rubanov, S., Dodd, A., and Saunders, M. (2018) Nanogeochemistry of hydrothermal magnetite. Contributions to Mineralogy and Petrology, 173.

Dupuis, C., and Beaudoin, G. (2011) Discriminant diagrams for iron oxide trace element fingerprinting of mineral deposit types. Mineralium Deposita, 46, 319-335.

Fenter, P., and Sturchio, N.C. (2004) Mineral–water interfacial structures revealed by synchrotron X-ray scattering. Progress in Surface Science, 77, 171-258.

Gottesmann, B., and Wirth, R. (1997) Pyrrhotite inclusions in dark pigmented apatite from granitic rocks. European Journal of Mineralogy, 491-500.

Heimann, A., Spry, P.G., Teale, G.S. (2005) Zincian spinel associated with metamorphosed Proterozoic base-metal sulfide occurrences, Colorado: a re-evaluation of gahnite composition as a guide in exploration. The Canadian Mineralogist, 43, 601-622.

Lanzillo, N., Watson, E., Thomas, J., Nayak, S., and Curioni, A. (2014) Near-surface controls on the composition of growing crystals: Car–Parrinello molecular dynamics (CPMD) simulations of Ti energetics and diffusion in alpha quartz. Geochimica et Cosmochimica Acta, 131, 33-46.

Li, L., Fijneman, A.J., Kaandorp, J.A., Aizenberg, J., and Noorduin, W.L. (2018) Directed nucleation and growth by balancing local supersaturation and substrate/nucleus lattice mismatch. Proceedings of the National Academy of Sciences of the United States of America, 115, 3575-3580.

Li, K., Pring, A., Etschmann, B., Macmillan, E., Ngothai, Y., O'Neill, B., Hooker, A., Mosselmans, F., and Brugger, J. (2015) Uranium scavenging during mineral replacement reactions. American Mineralogist, 100, 1728-1735.

Lilova, K.I., Pearce, C.I., Gorski, C., Rosso, K.M., Navrotsky, A. (2012) Thermodynamics of the magnetite-ulvospinel (Fe_3O_4-Fe_2TiO_4) solid solution. American Mineralogist, 97, 1330-1338.

Meng, F., Cui, M., Wu, X., Ren, Y. (2015) Heishan mafic–ultramafic rocks in the Qimantag area of Eastern Kunlun, NW China: Remnants of an early Paleozoic incipient island arc. Gondwana Research, 27, 745-759.

Nadoll, P., Angerer, T., Mauk, J.L., French, D., Walshe, J. (2014) The chemistry of hydrothermal magnetite: A review. Ore Geology Reviews, 61, 1-32.

Nadoll, P., Mauk, J.L., Hayes, T.S., Koenig, A.E., Box, S.E. (2017) Element partitioning in magnetite under low-grade metamorphic conditions–a case study from the Proterozoic Belt Supergroup, USA. European Journal of Mineralogy, 29, 795-805.

Putnis, A., Fernandez-Diaz, L., Prieto, M. (1992) Experimentally produced oscillatory zoning in the (Ba, Sr) SO_4 solid solution. Nature, 358, 743.

Sitzman, S.D., Banfield, J.F., Valley, J.W. (2000) Microstructural characterization of metamorphic magnetite crystals with implications for oxygen isotope distribution. American Mineralogist, 85, 14-21.

Stipp, S. (1999) Toward a conceptual model of the calcite surface: hydration, hydrolysis, and surface potential. Geochimica et Cosmochimica Acta, 63, 3121-3131.

Tooth, B., Ciobanu, C.L., Green, L., O'Neill, B., Brugger, J., 2011. Bi-melt formation and gold scavenging from hydrothermal fluids: An experimental study. Geochimica et Cosmochimica Acta, 75(19): 5423-5443.

Turnock, A., and Eugster, H. (1962) Fe—Al Oxides: Phase Relationships below 1,000 °C. Journal of Petrology, 3, 533-565.

Valentino, A., Carvalho, A., Sclar, C. (1990) Franklinite-magnetite-pyrophanite intergrowths in the Sterling Hill zinc deposit, New Jersey. Economic Geology, 85, 1941-1946.

Watson, E.B. (1996) Surface enrichment and trace-element uptake during crystal growth.

Geochimica et Cosmochimica Acta, 60, 5013-5020.

Watson, E.B. (2004). A conceptual model for near-surface kinetic controls on the trace-element and stable isotope composition of abiogenic calcite crystals1. Geochimica et Cosmochimica Acta, 68, 1473-1488.

Watson, E.B., and Müller, T. (2009) Non-equilibrium isotopic and elemental fractionation during diffusion-controlled crystal growth under static and dynamic conditions. Chemical Geology, 267, 111-124.

Wirth, R. (2009) Focused Ion Beam (FIB) combined with SEM and TEM: Advanced analytical tools for studies of chemical composition, microstructure and crystal structure in geomaterials on a nanometre scale. Chemical Geology, 261, 217-229.

Xu, Z.Q., Dilek, Y., Cao, H., Yang, J.S., Robinson, P., Ma, C.Q., Li, H.Q., Jolivet, M., Roger, F., and Chen, X.J. (2015) Paleo-Tethyan evolution of Tibet as recorded in the East Cimmerides and West Cathaysides. Journal Of Asian Earth Sciences, 105, 320-337.

Yin, S., Ma, C.Q., Robinson, P.T. (2017) Textures and high field strength elements in hydrothermal magnetite from a skarn system: Implications for coupled dissolution-reprecipitation reactions. American Mineralogist, 102, 1045-1056.

Figure captions

Figure 1. (a) A simplified tectonic outline of Qinghai-Tibet Plateau, modified from Xu et al. (2015); (b) The granitoid batholiths and related magmatic-hydrothermal deposits in

the East Kunlun orogenic belt, modified from Meng et al. (2013); (c) A simplified geological map of the Baishiya orefield, modified from Yin et al. (2017).

Figure 2. (a) The hand specimen of iron ores; (b) The selected magnetite crystals with euhedral morphology; (c) Photomicrograph of iron ores shows a mineral assemblage of phlogopite, magnetite, and hedenbergite; (d) BSE image of selected magnetite crystal consists of a homogeneous core and an oscillatory rim.

Figure 3. Trace element concentrations in the magnetite are determined by LA-ICP-MS and plotted with increasing compatibility into magnetite structure after Dare et al. (2014). The data source is from Yin et al. (2017).

Figure 4. STEM-ADF image and representative elemental mapping of the nanoscale lamellae using X-ray intensities of Mg-Kα, Al-Kα, O-Kα, Fe-Kα and Ti-Kα lines.

Figure 5. STEM-ADF image and a representative elemental mapping of the mineral nanoparticles using X-ray intensity of Si-Kα, Fe-Kα, O-Kα, Zn-Kα and Al-Kα lines.

Figure 6. STEM-ADF image and a representative elemental mapping of the mineral nanoparticles using X-ray intensity of O-Kα, Fe-Kα, Si-Kα, Al-Kα, Zn-Kα, Ti-Kα and Mg-Kα. Note that there are three phases: 1) Zn-Al-Mg-rich spinel phase; 2) Ti-rich

magnetite phase; 3) A pore inside the zinc spinel phase characterized by a depletion of oxygen (white circle). The size of these phases may be much smaller than the foil thickness (~100 nm).

Figure 7. (a) Energy filtered high-resolution lattice fringe image of the Mg-Al-rich lamella in host magnetite and (b) the related indexed diffraction pattern (fast Fourier Transform FFT). Note that there is split of the second order of the (111) reflections, suggesting two different spinel crystals with slightly different unit cell parameters. (c) The energy filtered high-resolution lattice fringe image of the Zn-Mg-Al-rich nanoparticle and the Ti-rich nanoparticle in the TEM foil of Fig. 3. (d) The indexed diffraction pattern (fast Fourier Transform FFT) from the different zones of the lattice fringe image. Note that the lattice parameters of the Ti-rich nanoparticle resemble those of the host magnetite because no additional spots have been observed in the related zone. However, a split can be observed when the Zn-Mg-Al-rich nanoparticle and the host magnetite have been involved.

Figure 8. The hercynite-magnetite solvus (Turnock and Eugster, 1962). The value of Al content marked in the arrow represents a total concentration of Al in the hercynite-magnetite series.

Figure 9. The spatial distribution of the Al-rich lamellae bearing magnetite (Phase 1), the

spotted nanoparticles bearing magnetite (Phase 2) and the relatively pure magnetite (Phase 3) in the foil. Note that their alternative variation is responsible for the oscillatory zoning on a micron scale of the magnetite rim.

Figure 10. (a) A zinc spinel nucleus nucleated and grown completely within the fluid phase; (b) A zinc spinel nucleus nucleated at the magnetite substrate. Note that the interfacial energy between magnetite and spinel nucleus is much lower than that between fluid phase and spinel nucleus (De Yoreo and Vekilov, 2003).

Figure 1

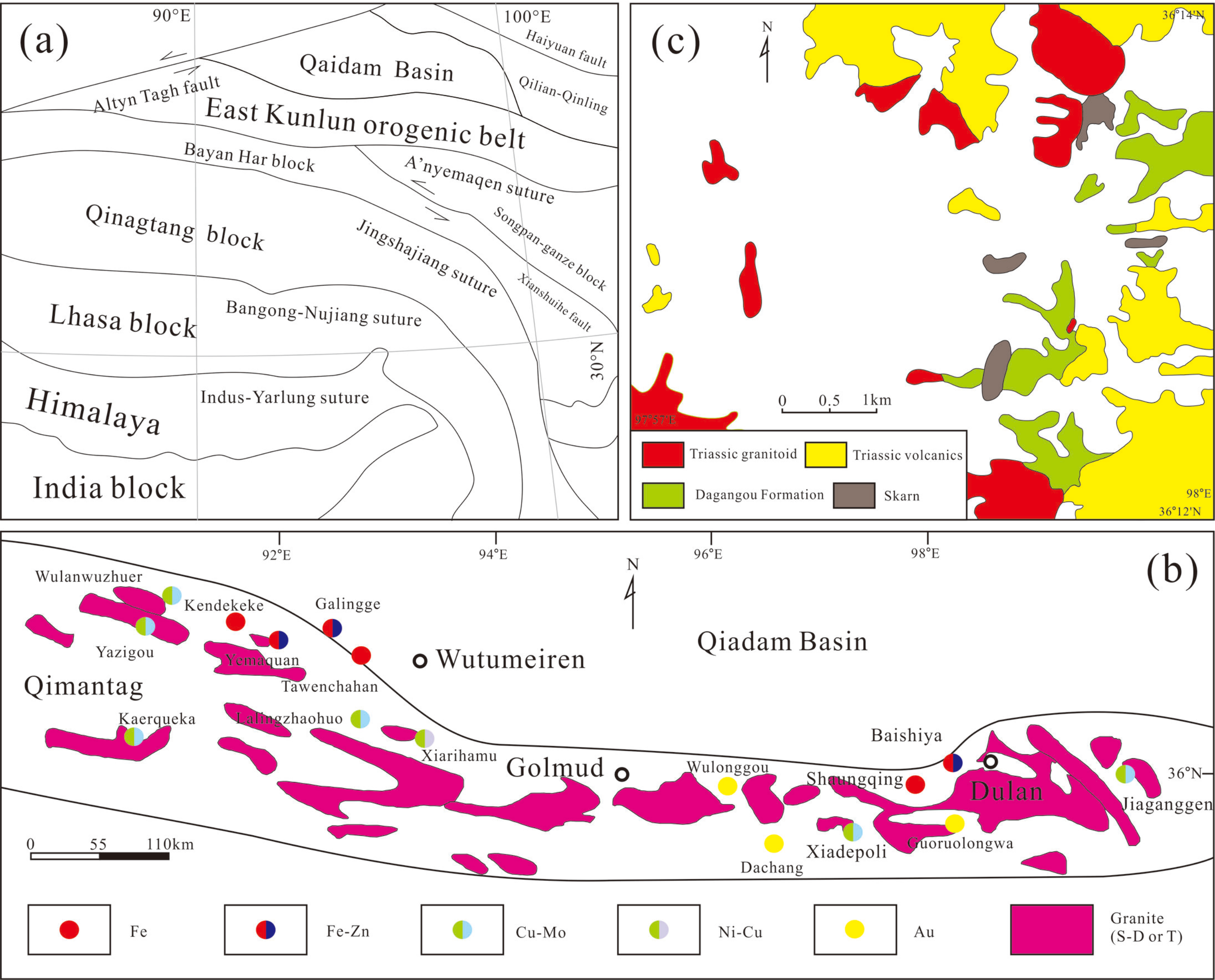
(a)
90°E
100°E
Haiyuan fault
Qaidam Basin
Qilian-Qinling
Altyn Tagh fault
East Kunlun orogenic belt
Bayan Har block
A'nyemaqen suture
Songpan-ganze block
Qinagtang block
Jingshajiang suture
Xianshuihe fault
Lhasa block
Bangong-Nujiang suture
30°N
Himalaya
Indus-Yarlung suture
India block
(c)
N
36°14'N
0 0.5 1km
97°57'E
98°E
36°12'N
Triassic granitoid
Triassic volcanics
Dagangou Formation
Skarn
(b)
92°E
94°E
96°E
98°E
N
Wulanwuzhuer
Kendekeke
Galingge
Yazigou
Yemaquan
Tawenchahan
Qimantag
Wutumeiren
Qiadam Basin
Kaerqueka
Lalingzhaohuo
Xiarihamu
Golmud
Baishiya
Wulonggou
Shaungqing
Dulan
36°N
Jiaganggen
0 55 110km
Xiadepoli
Guoruolongwa
Dachang
Fe
Fe-Zn
Cu-Mo
Ni-Cu
Au
Granite
(S-D or T)

Figure 2

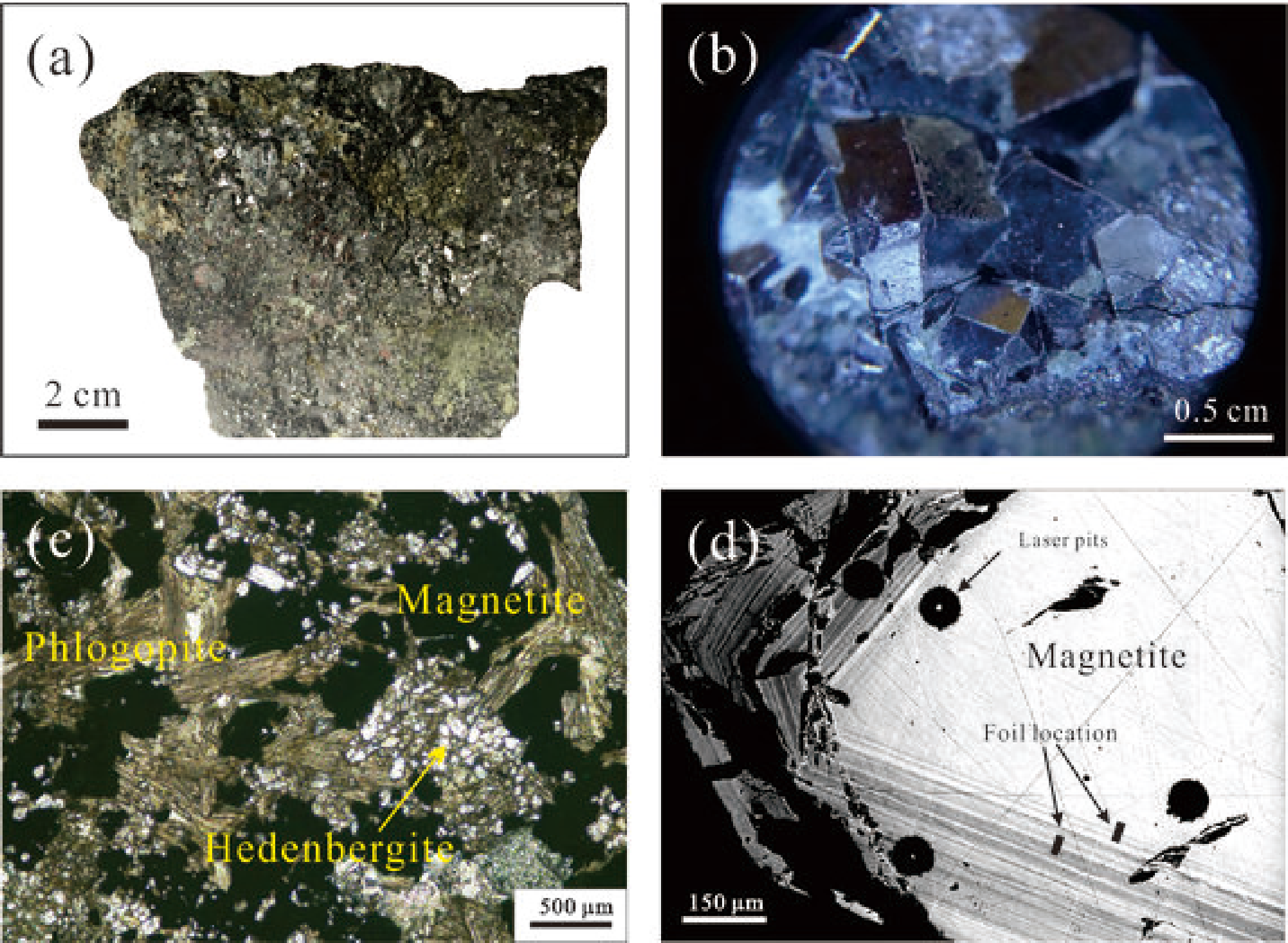
(a)
2 cm
(b)
0.5 cm
(c)
Magnetite
Phlogopite
Hedenbergite
500 µm
(d)
Laser pits
Magnetite
Foil location
150 µm

Figure 3

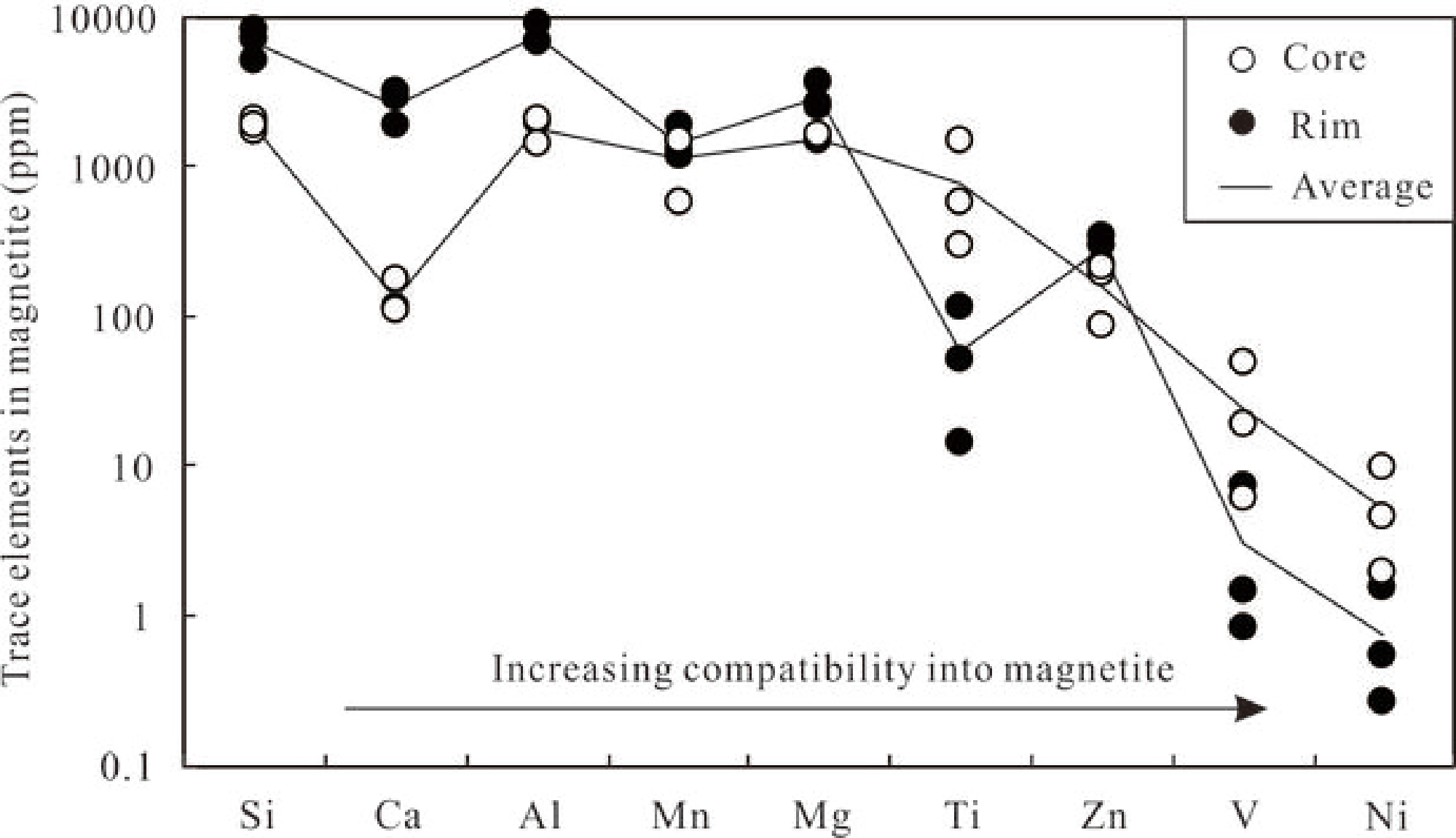
10000
1000
100
10
1
0.1
Trace elements in magnetite (ppm)
Core
Rim
Average
Increasing compatibility into magnetite
Si
Ca
Al
Mn
Mg
Ti
Zn
V
Ni

Figure 4

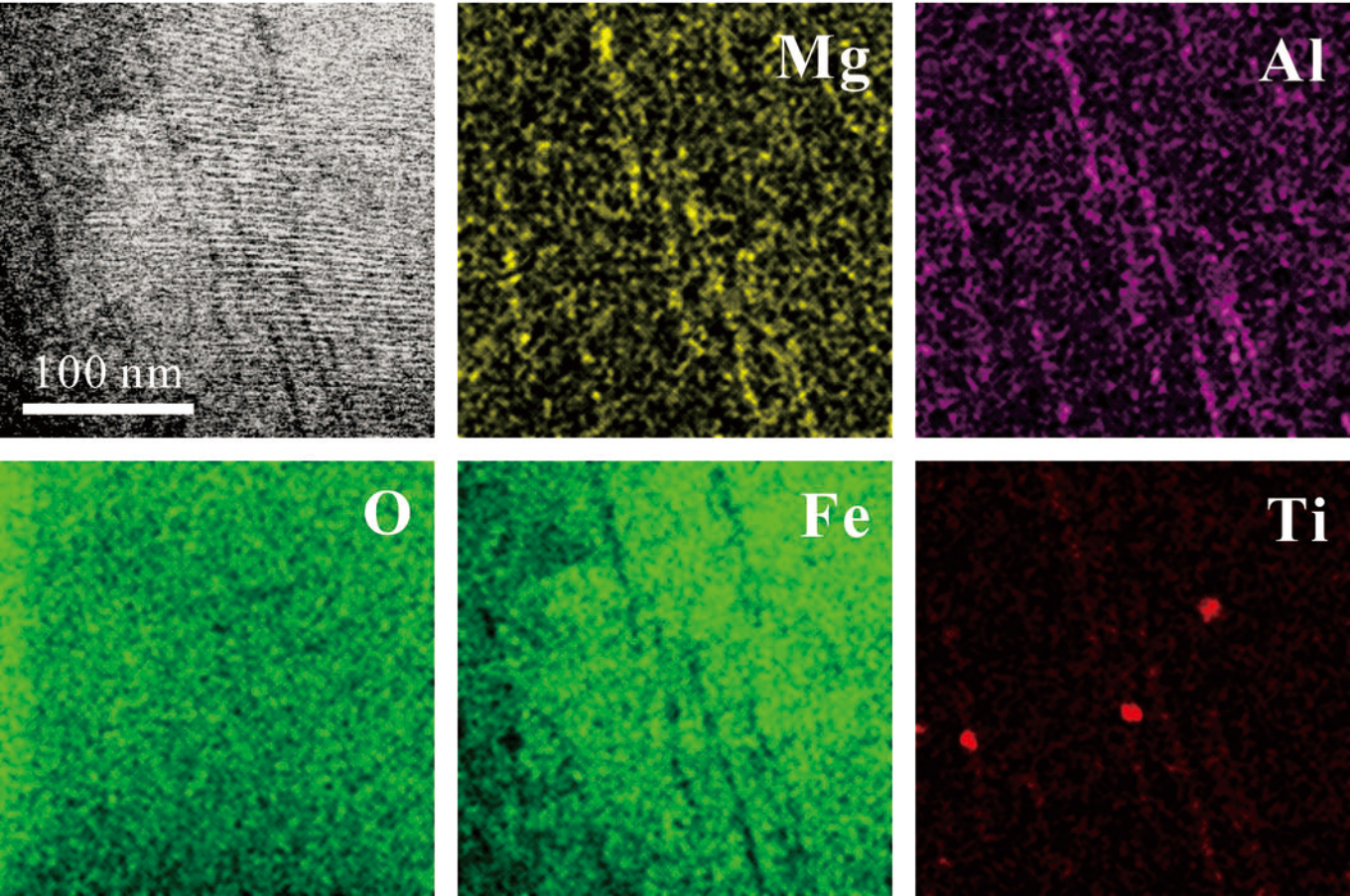

Figure 5

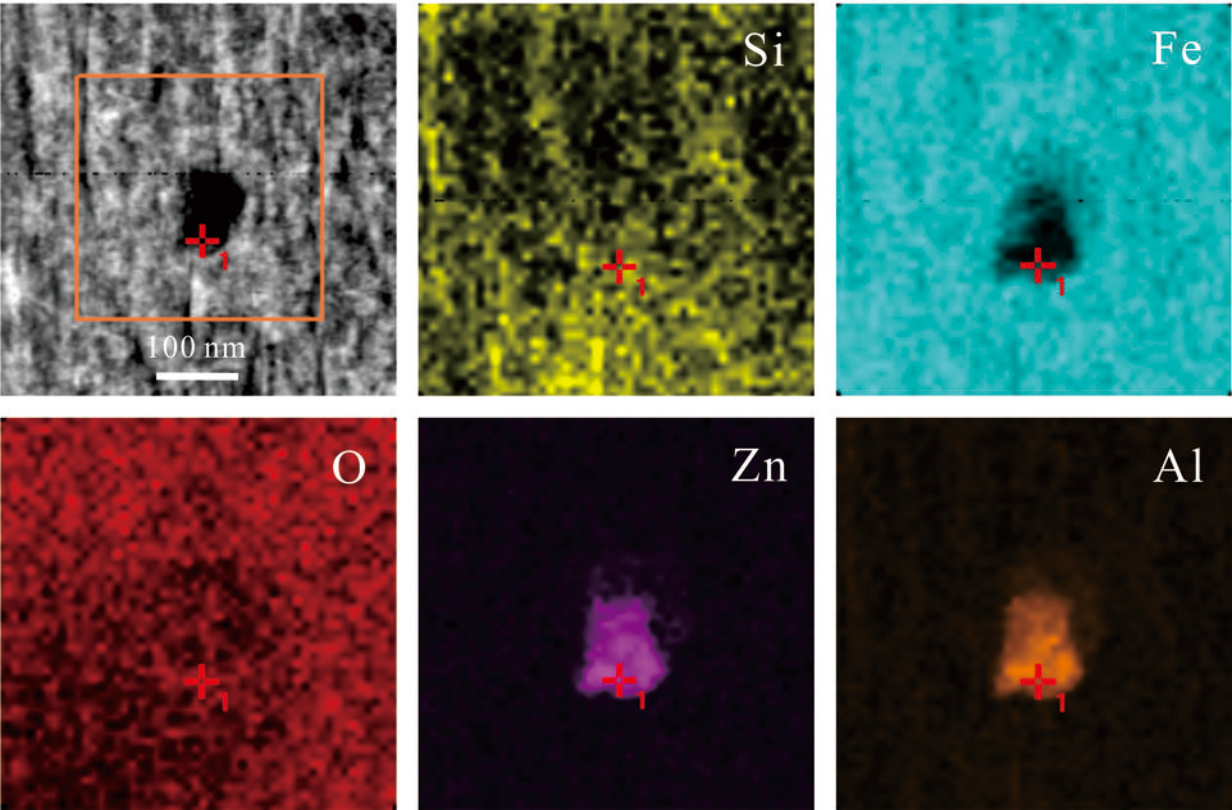

Figure 6

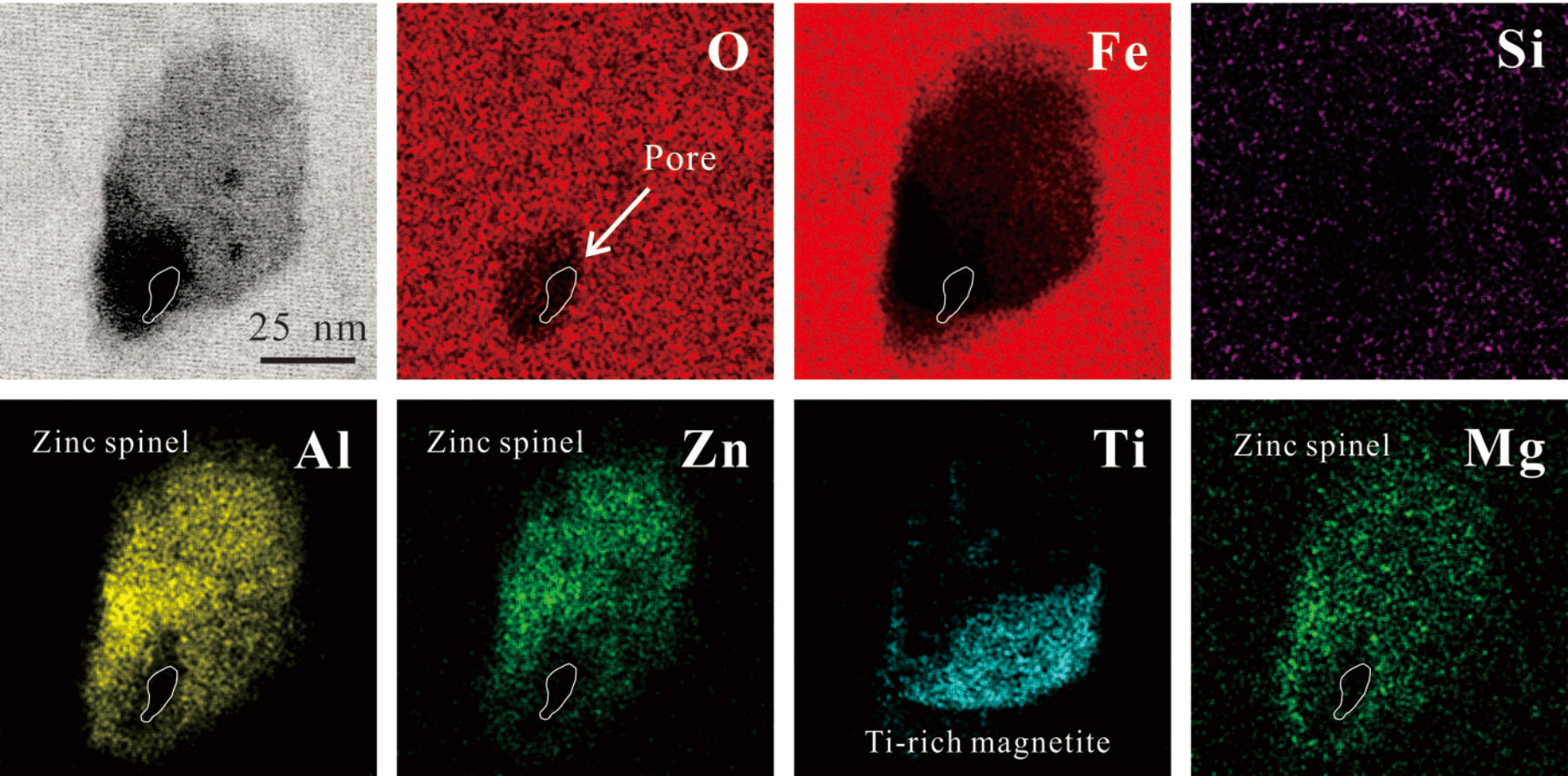
25 nm
O
Pore
Fe
Si
Zinc spinel
Al
Zinc spinel
Zn
Ti
Ti-rich magnetite
Zinc spinel
Mg

Figure 7

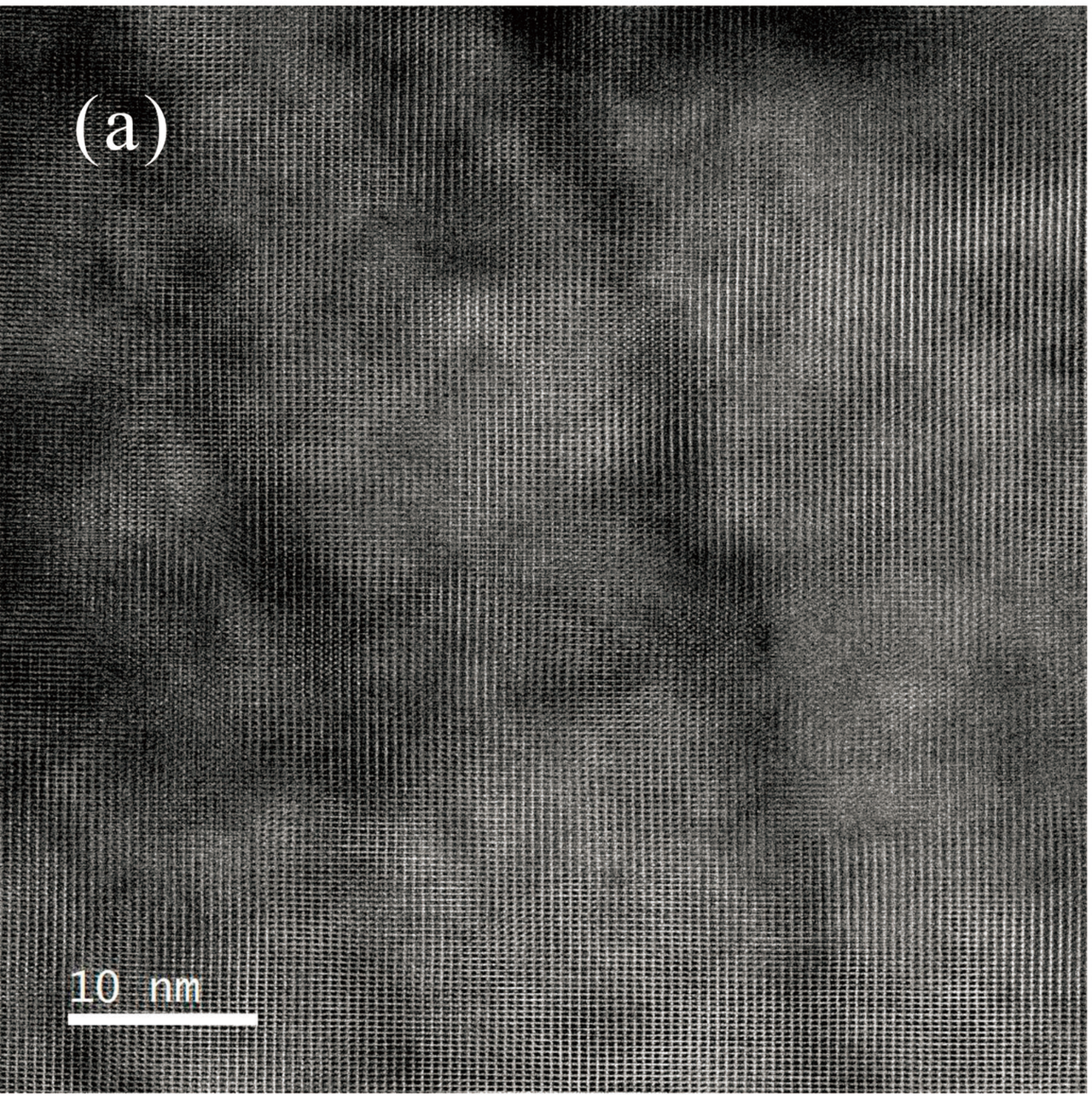
(a)
10 nm

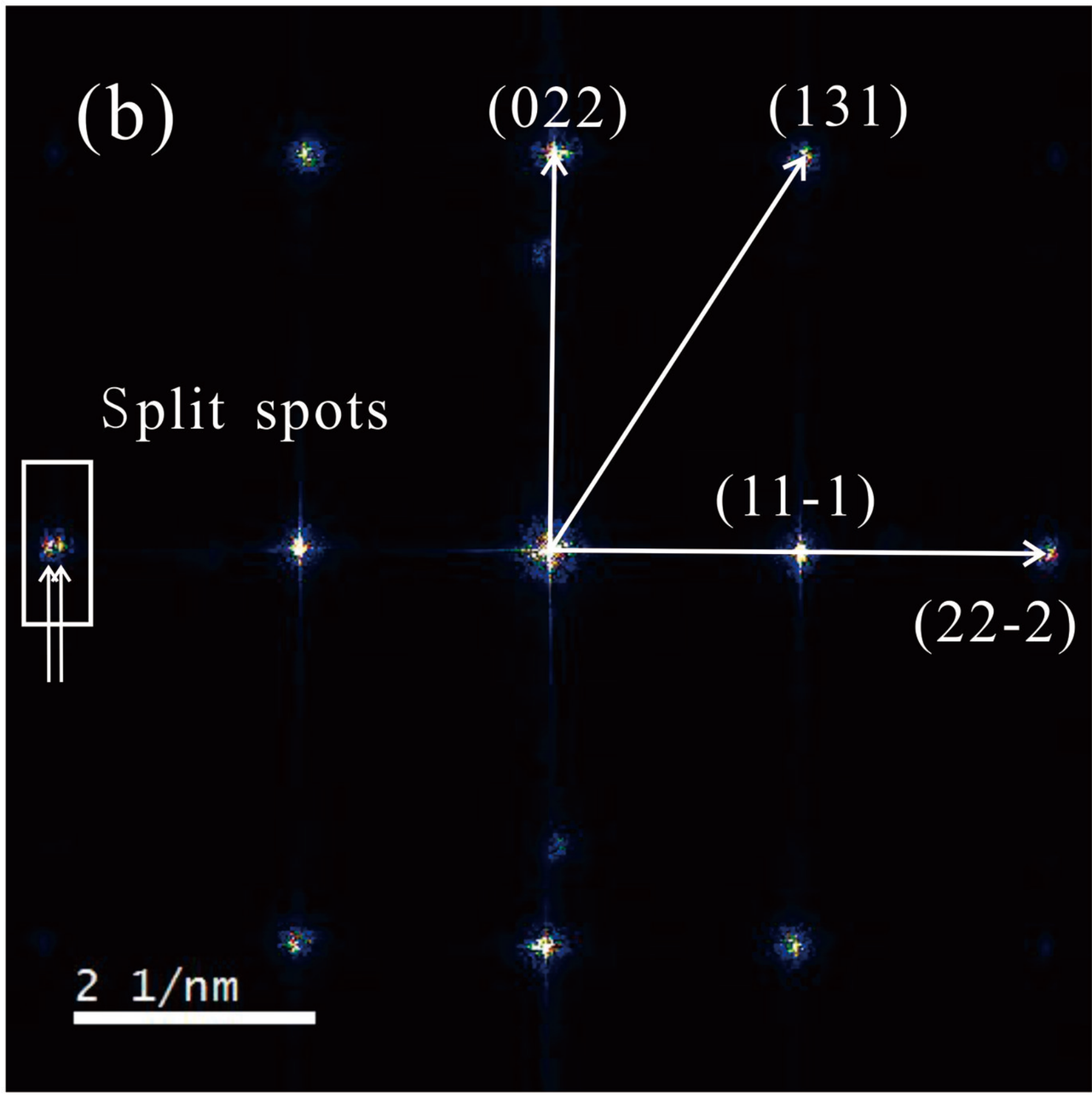
(b)
(022)
(131)
Split spots
(11-1)
(22-2)
2 1/nm

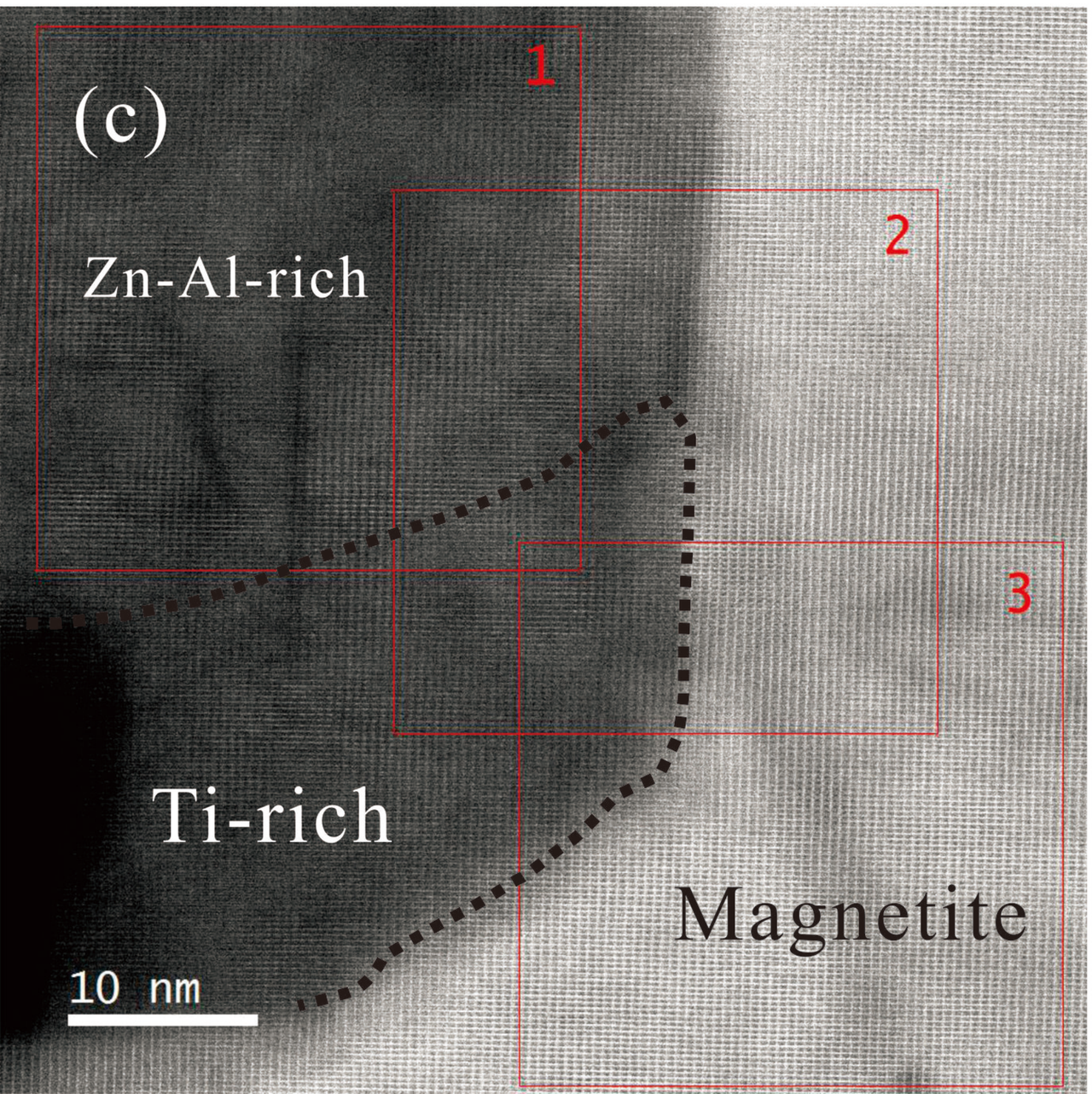
(c)
1
2
3
Zn-Al-rich
Ti-rich
Magnetite
10 nm

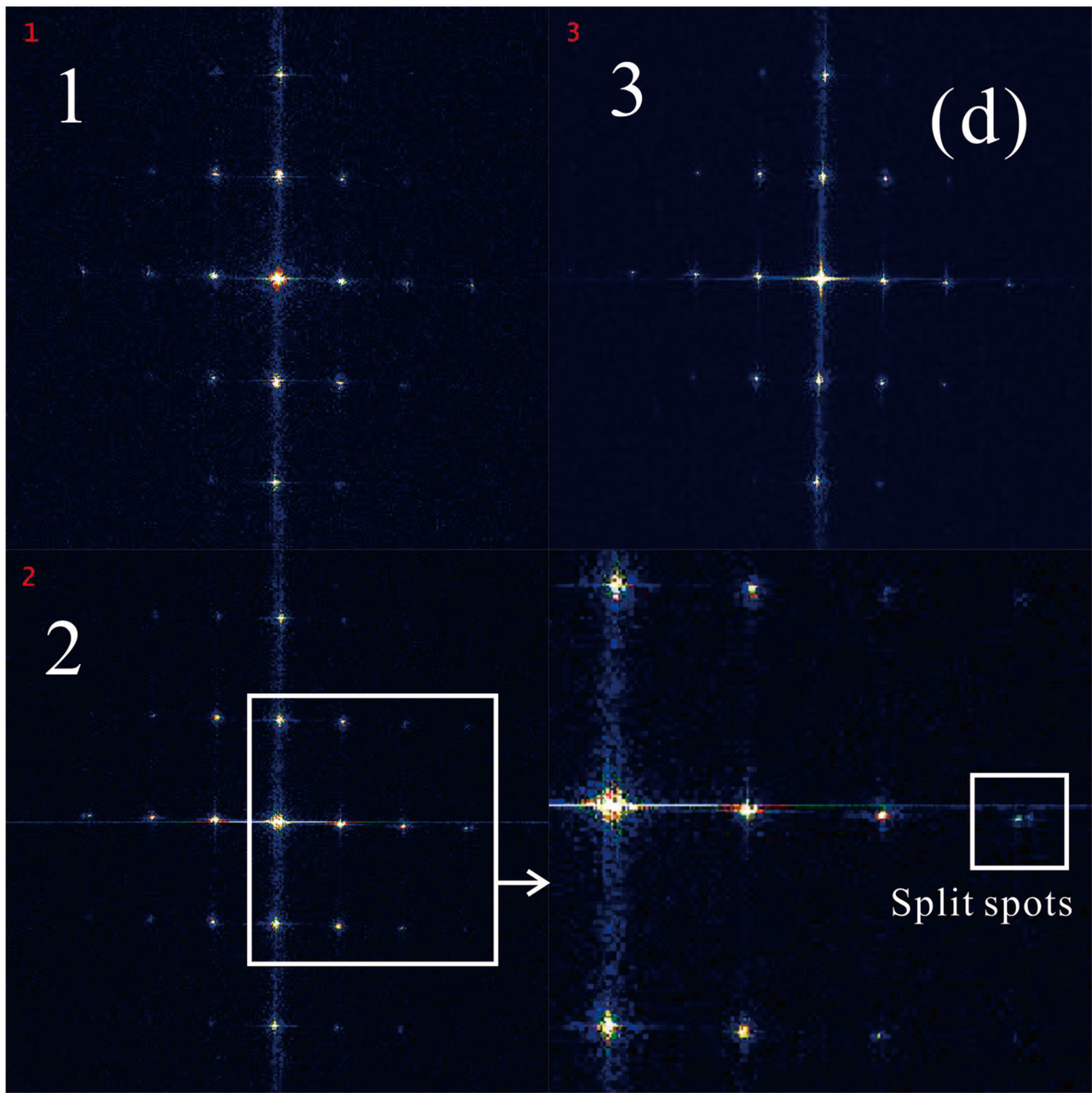
1
3
(d)
2
Split spots

Figure 8

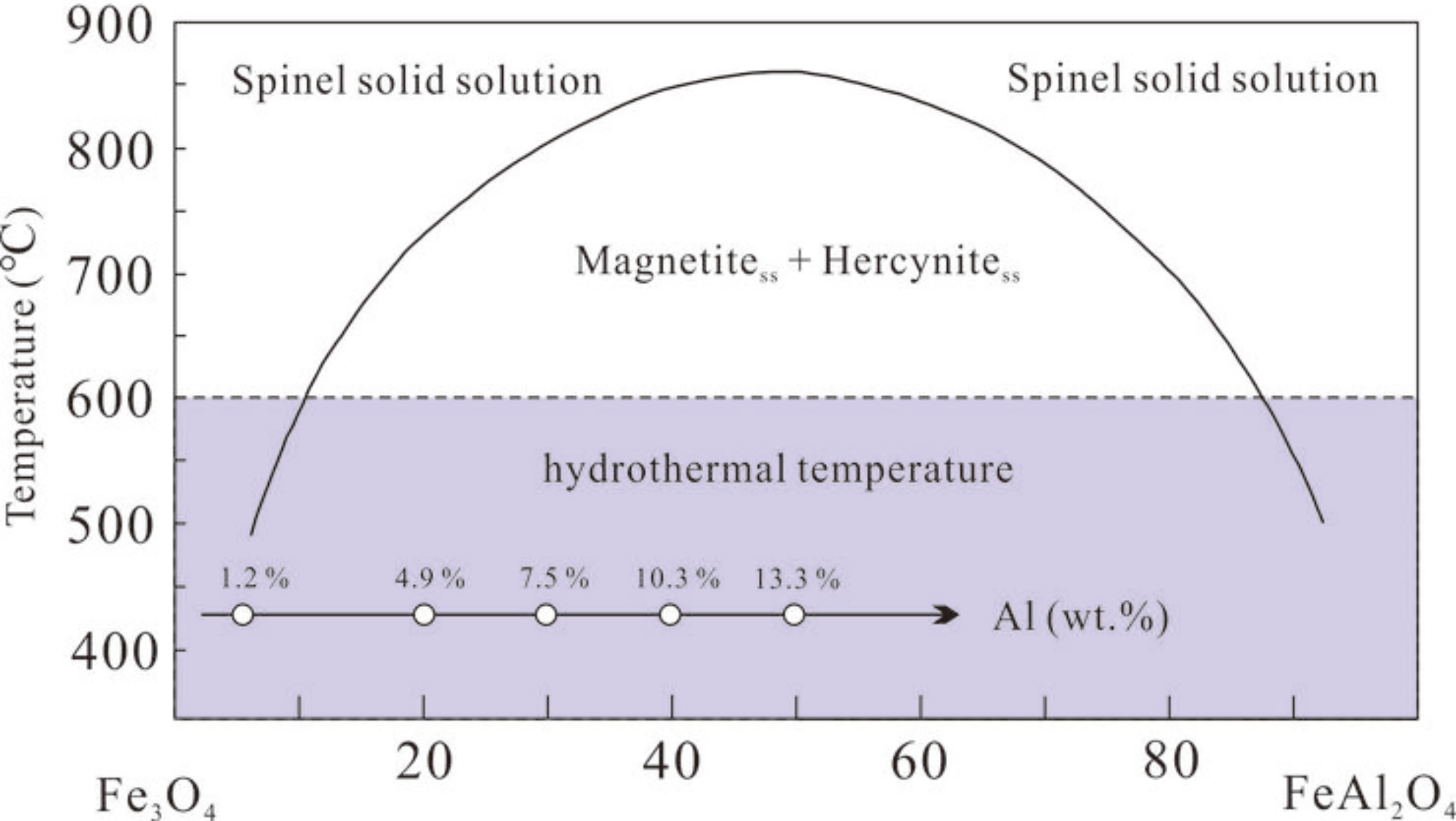
900
800
700
600
500
400
Temperature (°C)
Spinel solid solution
Spinel solid solution
Magnetite$_{ss}$ + Hercynite$_{ss}$
hydrothermal temperature
1.2 %
4.9 %
7.5 %
10.3 %
13.3 %
Al (wt.%)
20
40
60
80
Fe_3O_4
$FeAl_2O_4$

Figure 9

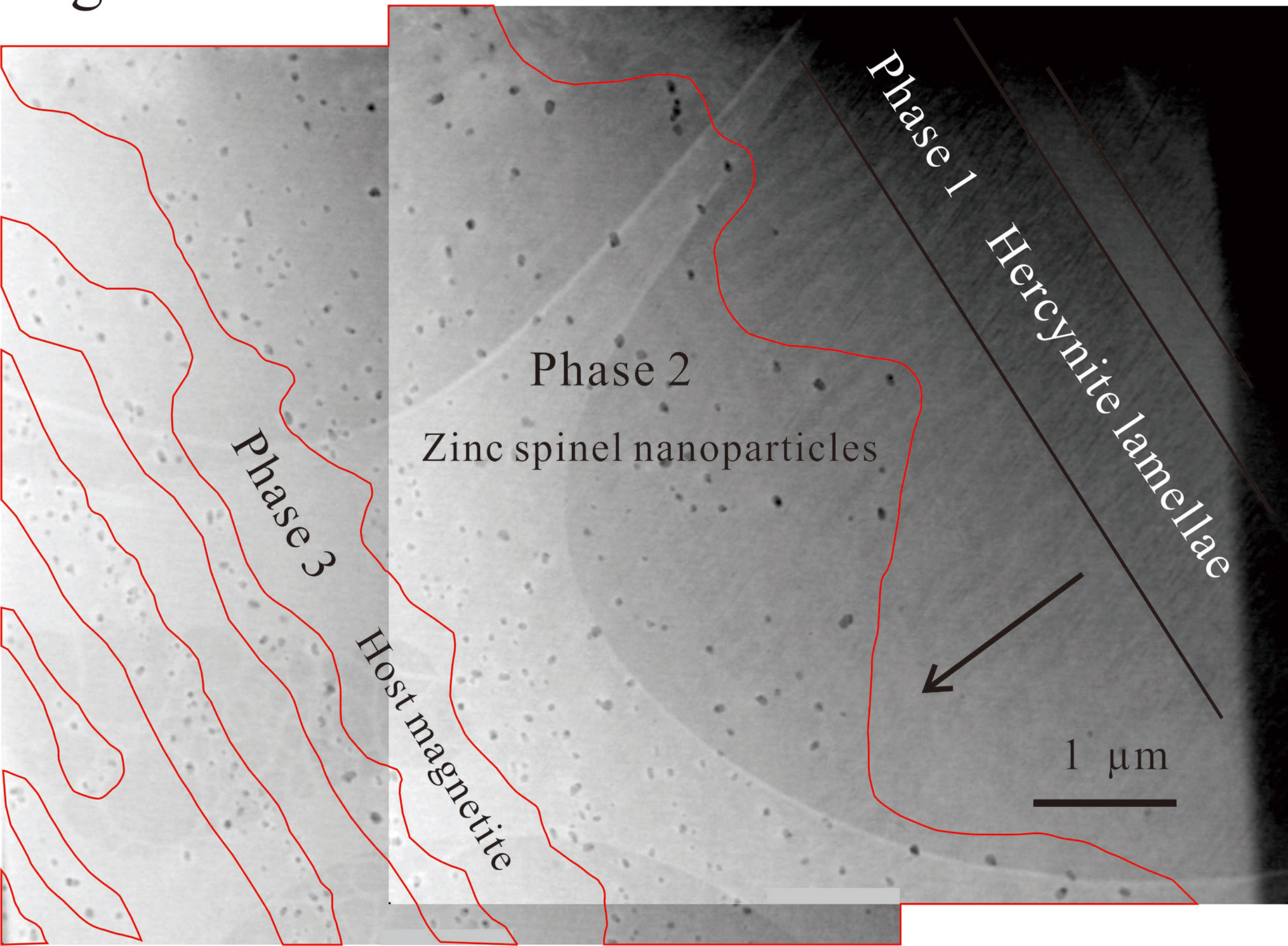
Phase 1
Hercynite lamellae
Phase 2
Zinc spinel nanoparticles
Phase 3
Host magnetite
1 μm

Figure 10

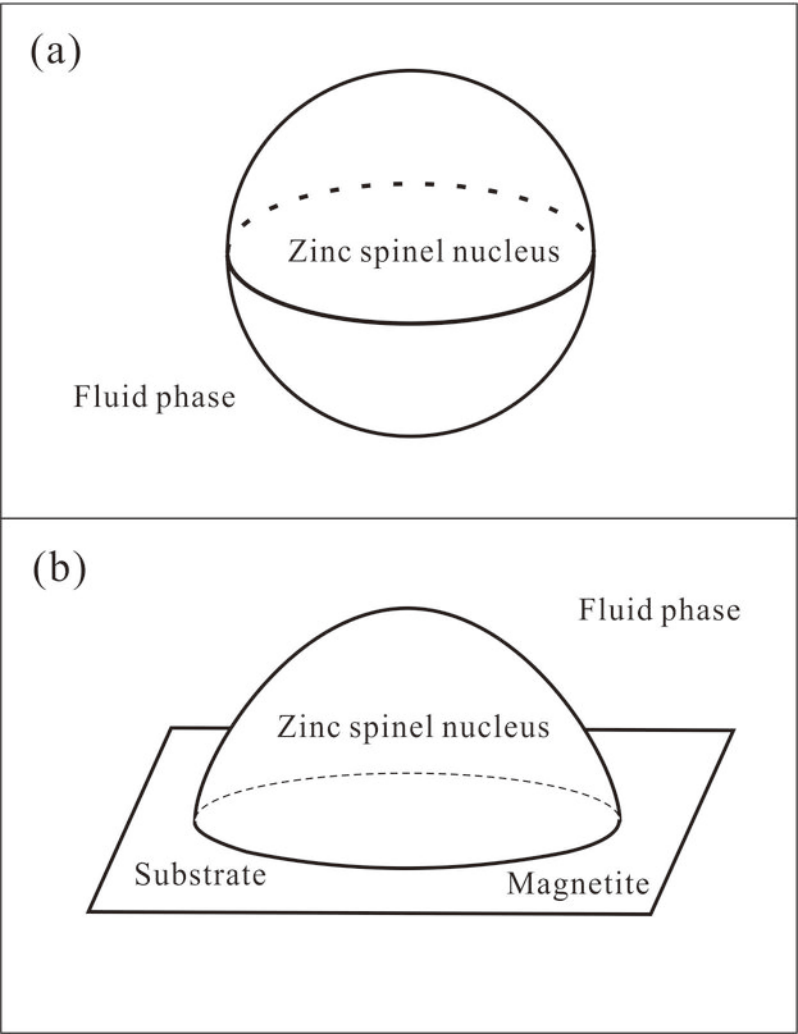
(a)
Zinc spinel nucleus
Fluid phase
(b)
Fluid phase
Zinc spinel nucleus
Substrate
Magnetite